# Impact of Global Warming on the Western North Pacific Circulation Anomaly during Developing El Niño

YUHAO WANG

*Key laboratory of Meteorological Disaster, Ministry of Education/Joint International Research Laboratory of Climate and Environmental Change/Collaborative Innovation Center on Forecast of Meteorological Disasters, Nanjing University of Information Science and Technology, Nanjing, China*

CHAO HE

*Institute for Environmental and Climate Research, Jinan University, Guangzhou, China*

TIM LI

*Key laboratory of Meteorological Disaster, Ministry of Education/Joint International Research Laboratory of Climate and Environmental Change/Collaborative Innovation Center on Forecast of Meteorological Disasters, Nanjing University of Information Science and Technology, Nanjing, China, and International Pacific Research Center and Department of Atmospheric Sciences, School of Ocean and Earth Science and Technology, University of Hawai'i at Mānoa, Honolulu, Hawaii*

(Manuscript received 1 August 2019, in final form 12 November 2019)

ABSTRACT

El Niño stimulates an anomalous cyclone over the North Pacific during its developing phase. Using 30 CGCMs and 11 AGCMs from CMIP5, we find a weakly strengthened anomalous North Pacific cyclone (NPC) in a warmer climate in CGCMs, and intermodel uncertainty exists. A similar change of the anomalous NPC is found in AGCMs with increased mean state SST but with a stronger amplitude of enhancement. Based on a simple Gill model, the diabatic heating anomaly, mean state static stability, and meridional gradient of relative vorticity are identified to be responsible for the change of the anomalous NPC. Analyses of the CMIP5 models suggest that the change of the anomalous NPC is largely determined by the competition between the enhanced diabatic heating anomaly and the enhanced mean state static stability. The amplitude of enhancement of the anomalous NPC is strongly modulated by the change of precipitation anomaly over the equatorial central-eastern Pacific, which depends on the changes of mean state SST and the El Niño–related SST anomaly. Compared with a uniform warming, an El Niño–like mean state SST warming favors a much stronger enhancement of the anomalous NPC, by enhancing the mean state precipitation and latent heating anomaly associated with the precipitation anomaly over the equatorial Pacific. However, the air–sea coupling acts to weaken the SST anomaly associated with El Niño in the CGCMs, which further reduces the enhancement of the anomalous NPC.

## 1. Introduction

At interannual time scale, El Niño–Southern Oscillation is the dominant signal in the tropics, and it has a profound impact on global climate (Rasmusson and Carpenter 1982; Webster and Yang 1992; Webster et al. 1998; Alexander et al. 2002). Through atmospheric teleconnections, El Niño can remotely modulate the climate variability over the northwest Pacific peripheral regions (Wang et al. 2000; Wang et al. 2003; Li et al. 2018; Zhang et al. 2017; Jiang and Li 2018), leading to meteorological disasters, such as floods (Zong and Chen 2000), droughts (Keil et al. 2008; Zhang et al. 2014), and haze (Li et al. 2017; Zhao et al. 2018; He et al. 2019c). Thus understanding the variability of the El Niño–related atmospheric anomalies is of great economic and societal value.

Forced by the positive sea surface temperature (SST) anomaly over the equatorial central-eastern Pacific, an

Supplemental information related to this paper is available at the Journals Online website: https://doi.org/10.1175/JCLI-D-19-0588.s1.

*Corresponding author*: Dr. Chao He, hechao@jnu.edu.cn

DOI: 10.1175/JCLI-D-19-0588.1

anomalous cyclone is stimulated over the North Pacific during the developing phase of El Niño, which is the prominent circulation system over the western North Pacific (WNP) (Wang et al. 2003; Li et al. 2018). During the summer of developing El Niño, the western edge of the anomalous North Pacific cyclone (NPC) could extend westward to East Asia and directly weaken the East Asian summer monsoon, resulting in deficient precipitation over eastern China (Wu et al. 2003). Meanwhile, the WNP monsoon trough extends westward, which increases the geneses of the tropical cyclone (TC) over the southeast quadrant of the tropical Pacific (Chen et al. 1998; Wang and Chan 2002). The anomalous NPC is also the key bridge for the formation of the anomalous western North Pacific anticyclone (Li et al. 2018; Wu et al. 2017b). Modulated by the seasonal transition of the mean state, the western branch of the anomalous NPC withdraws eastward gradually during the developing phase of El Niño (Wu et al. 2017b). The northeasterly wind over the western branch of the anomalous NPC interacts with the local SST through the wind–evaporation–SST feedback (Wang et al. 2000) or advects an air mass with negative moist enthalpy into the near-equatorial WNP (Wu et al. 2017a), giving rise to the formation of the anomalous anticyclone, which could further modulate the East Asian climate variability (Wang et al. 2000; Li et al. 2018; Zhang et al. 2017).

Given the great impact of global warming on climate variability, great effort has been devoted to detect how ENSO's teleconnections may change in the future (e.g., Kug et al. 2010; Zhou et al. 2014; Perry et al. 2017; Jiang et al. 2018; He et al. 2019b). Kug et al. (2010) suggested the eastward shift of ENSO's teleconnection over the North Pacific–American based on multiple coupled general circulation models (CGCMs), and Zhou et al. (2014) proposed that ENSO-forced Pacific–North American (PNA) teleconnection pattern will intensify and move eastward in the future during El Niño mature winter based on atmospheric-only models. Perry et al. (2017) investigated the future changes of ENSO temperature and precipitation teleconnections over global land area during boreal winter, and found that spatial extents of the above teleconnections increase robustly. Both Jiang et al. (2018) and He et al. (2019b) indicated a weakened anomalous western North Pacific anticyclone during the summer of decaying El Niño, possibly through the change in SST anomaly over the WNP associated with the local air–sea interaction (Jiang et al. 2018) or the weakened impact of the tropical Indian Ocean on the atmosphere (He et al. 2019b). While the mechanisms controlling the variability of the atmospheric circulation anomaly are different during different El Niño phases (Li et al. 2018), it is still unclear how the global warming will modulate the WNP circulation anomaly during the developing phase of El Niño.

To understand the impact of the global warming on the WNP circulation anomaly during the developing phase of El Niño, ensemble simulation by fully coupled GCMs is needed to suppress the stochastic oscillation generated by internal variability (Deser et al. 2012; Xie et al. 2015). The possible response of the anomalous circulation over the WNP to global warming may be affected by the change in the SST anomaly associated with El Niño or the sensitivity of the atmosphere to the SST anomaly. It is suggested that the response of ENSO amplitude to global warming suffers larger uncertainty (Collins et al. 2010; Chen et al. 2015; Maher et al. 2018). Even if the ENSO amplitude is unchanged in the future, the precipitation anomaly over the tropical Pacific becomes stronger (Power et al. 2013; Cai et al. 2014), which can further modulate the atmospheric circulation anomalies. In the current study, we focus on the behavior of the anomalous NPC during the autumn of developing El Niño and aim to answer the following questions: 1) How will the global warming impact the response of the anomalous NPC to El Niño? 2) What underlying physical mechanisms are responsible for the change of the anomalous NPC?

The rest of paper is organized as follows. The model, data, and methods are described in section 2. The simulated WNP atmospheric anomalies during the autumn of developing El Niño are evaluated against the observation in section 3. Section 4 investigates the response of the anomalous NPC to global warming in CGCMs and atmospheric general circulation models (ACGMs). A theoretical model is adopted to thoroughly understand the mechanisms for the responses simulated by CGCMs and AGCMs in section 5, and the mechanisms for the amplitude of change in the precipitation anomaly over the equatorial central-eastern Pacific are investigated in section 6. Finally, conclusions and a discussion are presented in section 7.

## 2. Model, data, and methods

### *a. Models*

In total 30 CGCMs from phase 5 of the Coupled Model Intercomparison Project (CMIP5; Taylor et al. 2012) are adopted for analyses in the current study (listed in Table S1 in the online supplemental material with brief descriptions). The monthly outputs of the Historical and the representative concentration pathway 8.5 (RCP8.5) experiments are adopted for analyses, and only one realization for each model is used to give equal weight. The Historical experiment of the CMIP5

models is performed by forcing the CGCMs with observed historical external forcing, while the RCP8.5 experiment is forced by a high-emission pathway toward a radiative forcing of 8.5 W $m^{-2}$ in the year 2100 (van Vuuren et al. 2011). The RCP8.5 experiment is compared to the Historical experiment to extract the GHG-forced responses. The 1950–99 period in the Historical experiment is adopted as the baseline climate (20C), and the 2050–99 period in the RCP8.5 experiment is considered as the future climate (21C).

To investigate whether the change of the El Niño–related SST anomaly is necessary for the change of the anomalous NPC, the AMIP, AMIP4K, and AMIPFuture experiments based on the AGCMs participating in CMIP5 (the 11 boldface models in Table S1) are analyzed. The AMIP experiment is referred to as 20C and the AMIP4K/AMIPFuture experiments is referred to as 21C. The AMIP experiment is forced by the observed monthly SST evolution for 1979–2008. The underlying SST pattern in the AMIP4K experiment is obtained by adding a globally uniform SST warming of 4 K to the observed SST, while the underlying SST pattern in the AMIPFuture experiment is the observed SST plus a patterned SST warming derived from the CMIP3 multimodel ensemble mean of quadrupling $CO_2$ simulation (Bony et al. 2011; Taylor et al. 2012; Zhou et al. 2014). Since the interannual variability of the SST anomalies is exactly the same in the three experiments, the differences between AMIP and AMIP4K experiments indicate the modulation of global warming on the interannual climate variability while keeping the El Niño–related SST anomaly unchanged, and a comparison between AMIPFuture and AMIP4K experiments tells whether the warming pattern of the mean state SST can modulate the interannual climate variability.

### b. *Observation data*

The following reanalysis and observational data are adopted in this study: 1) the monthly atmospheric variables from NCEP–NCAR reanalysis (Kalnay et al. 1996), including horizontal wind and geopotential height [note that streamfunction $\psi$ is calculated from horizontal wind vector, and the eddy geopotential height ($H_e$) is calculated by removing the simultaneous tropical–subtropical (0°–25°N) mean geopotential height (He et al. 2018)]; 2) the monthly SST derived from Extended Reconstructed SST version 5 (B. Huang et al. 2017); and 3) the gridded precipitation derived from the Global Precipitation Climatology Project (GPCP) version 2.3 (Adler et al. 2003).

### c. *Methods*

All the observational and model data are bilinearly interpolated onto a 2.5° × 2.5° horizontal grid. An 8-yr high-pass Fourier filter is applied to all the data to extract interannual variability. In this study, we focus on boreal autumn [September–November (SON)]. The ENSO index is defined as the regional averaged SST anomaly over the Niño-3.4 region (5°S–5°N, 170°–120°W). Due to the large uncertainty in the response of ENSO amplitude change to global warming (Collins et al. 2010; Chen et al. 2015; Maher et al. 2018), we mainly investigate the sensitivity of the atmospheric anomalies to the El Niño–related SST anomaly. First, all the atmospheric anomalies are regressed onto the contemporary unstandardized ENSO index, and the regression slope is calculated at each grid for each model. Second, the multimodel median (MMM) is obtained at each grid among the models. For the change of the atmospheric circulation indexes, the values of the indexes are calculated for each model before the MMM is obtained. We also examine the results based on the multimodel mean (Figs. S1–S3), which are similar to MMM. Since the median is more robust and less affected by outliers based on previous studies (Gleckler et al. 2008; Naughten et al. 2018), we mainly show the results based on the MMM. According to Power et al. (2012), 68% of intermodel consensus on the sign of the change equals the 95% confidence level of the Student's $t$ test, and a tighter threshold of 70% intermodel consistency is adopted in the current study.

## 3. Observed and simulated atmospheric anomalies over the western North Pacific during the autumn of developing El Niño

Figure 1 shows the observed and simulated atmospheric anomalies during the autumn of developing El Niño. The negative $H_e$ anomalies extend from about 130°E to eastern Pacific, with a large anomalous cyclone appearing over the North Pacific (Fig. 1a), which is the prominent circulation system during developing El Niño over the WNP. The northerly wind over the western branch of the anomalous NPC interacts with the local SST through the wind–evaporation–SST feedback (Wang et al. 2000) or advects air mass with negative moist enthalpy into the near-equatorial WNP (Wu et al. 2017a), leading to the formation of the anomalous anticyclone over the South China Sea (SCS), characterized by the positive $H_e$ anomalies (Fig. 1a). As shown in Fig. 1b for the streamfunction anomalies, the WNP and the SCS are characterized by negative and positive streamfunction anomalies respectively, corresponding to the anomalous NPC and anticyclone. Forced by the warm underlying SST anomaly, the equatorial central-eastern Pacific is occupied by the strong precipitation anomaly (Fig. 1b), and the strong latent heating anomaly released by the anomalous precipitation drives the atmospheric teleconnections

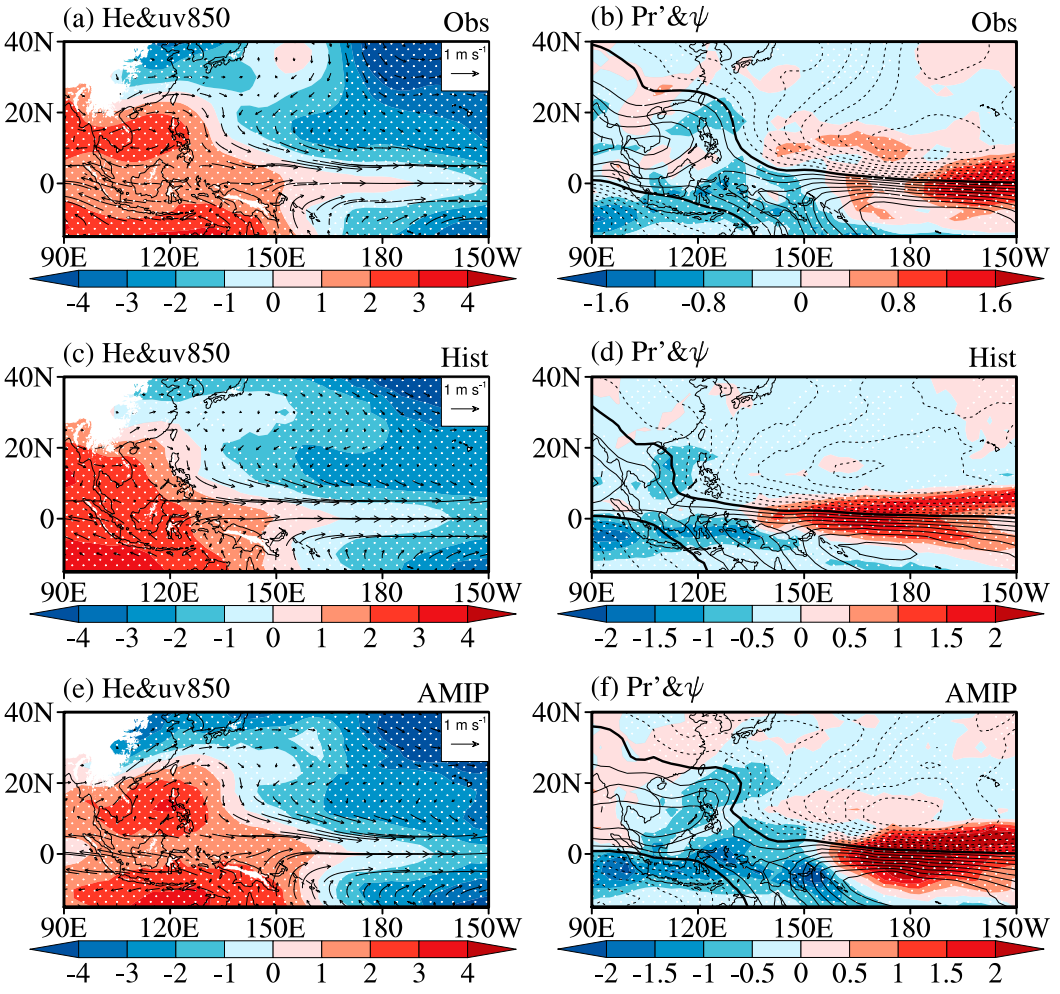


FIG. 1. Regressed anomalies during the autumn of developing El Niño onto the simultaneous Niño-3.4 index for (top) observation, (middle) the Historical experiment, and (bottom) the AMIP experiment. The regressed anomalies are (left) eddy geopotential height ($H_e$; gpm) and wind (m s$^{-1}$) at 850 hPa and (right) streamfunction (contours; $10^6$ m$^2$ s$^{-1}$) at 850 hPa and precipitation (shading; mm day$^{-1}$). The contours in the right panel are from $-2.4 \times 10^6$ to $1.6 \times 10^6$ m$^2$ s$^{-1}$ with an interval of $0.2 \times 10^6$ m$^2$ s$^{-1}$, and negative contours are dashed. The regressed anomalies significant at the 95% confidence level are stippled.

and is responsible for the remote impacts of ENSO (Hoskins and Karoly 1981; Trenberth et al. 1998; Chiang and Sobel 2002).

Previous studies have suggested that the models could generally capture the major atmospheric anomalies during El Niño (e.g., Zhou et al. 2014; Perry et al. 2017; He et al. 2019b). The anomalous WNP circulations simulated by the CGCMs and AGCMs are shown in Figs. 1c–f based on the MMM. Compared to the observation, the AGCMs and CGCMs could capture the major atmospheric anomalies, including the anomalous NPC, the associated positive precipitation anomaly, and easterly wind anomalies over the equatorial Pacific. The major bias is that the anomalous NPC and the easterly wind anomalies over the equatorial Pacific extends relatively westward as well as the associated positive precipitation anomaly, especially in the CGCMs. Overall, the similarity between the simulated circulation pattern and the observation suggests that the models have the capability of capturing the major observed climate variability during the autumn of developing El Niño, giving us confidence to further investigate the response of the anomalous NPC to global warming.

## 4. Responses of the anomalous North Pacific cyclone to global warming in CGCMs and AGCMs

Figure 2 shows the responses of $H_e$, streamfunction, wind at 850 hPa, and precipitation anomalies during the

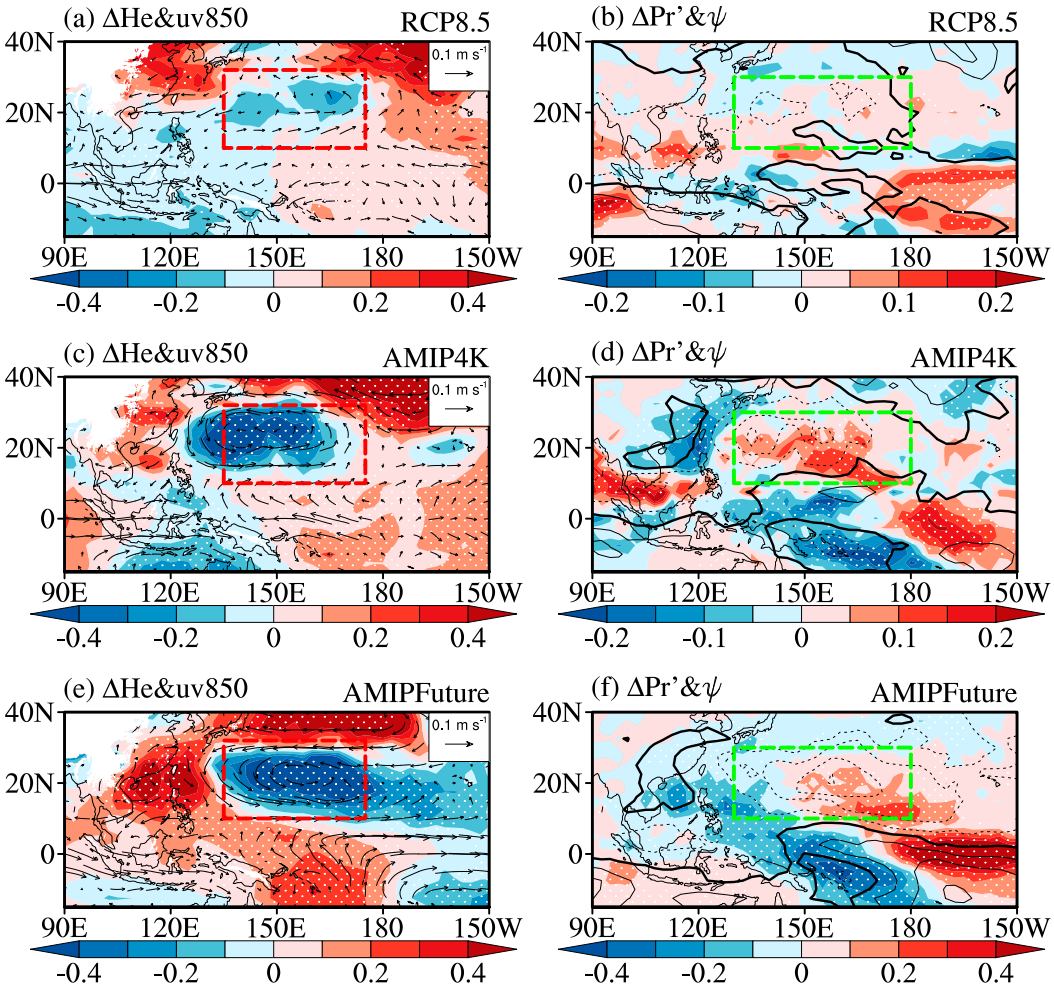


FIG. 2. The projected change of the regressed anomalies as shown in Fig. 1 scaled by the tropical (30°S–30°N) mean SST warming in the (top) RCP8.5, (middle) AMIP4K, and (bottom) AMIPFuture experiments. The contours in the right panel are from $-0.3 \times 10^6$ to $0.3 \times 10^6\,m^2\,s^{-1}$ with an interval of $0.05 \times 10^6\,m^2\,s^{-1}$, and negative contours are dashed. The changes agreeing with at least 70% of the individual models are stippled. The red (10°–32°N, 135°–175°E) and green (10°–30°N, 130°–180°E) boxes are the key regions selected to define the $H_e$ index and the $\psi$ index.

autumn of developing El Niño in RCP8.5, AMIP4K, and AMIPFuture experiments, in terms of the MMM for each experiment. All the changes are scaled by the tropical (30°S–30°N) mean SST warming values, which are 2.5, 4.0, and 4.8 K for the RCP8.5, AMIP4K, and AMIPFuture experiments respectively. Compared to the 20C, weakly enhanced negative $H_e$ anomalies appear over the WNP but agree with less than 70% of the individual models, accompanied with an anomalous cyclone (Fig. 2a) and enhanced negative streamfunction anomalies (contours in Fig. 2b). The above multiple metrics consistently indicate a weak enhancement of the anomalous NPC in the MMM. The positive precipitation anomaly over the equatorial Pacific on the east of the date line is robustly strengthened, resulting in the robust enhancement of the diabatic heating anomaly. As the anomalous NPC is directly forced by the diabatic heating anomaly over the equatorial central-eastern Pacific (Wang et al. 2000; Li et al. 2018; Wu et al. 2017b), it raises a question as to why the robustly enhanced diabatic heating anomaly results in a weakly enhanced anomalous NPC in the RCP8.5 experiment.

In the AMIP4K and AMIPFuture experiments (Figs. 2c–f), the changes of the atmospheric anomalies during the autumn of developing El Niño share a similar pattern with the RCP8.5 experiment but with a generally stronger enhancement. The difference of the atmospheric circulation anomalies between 21C and 20C in AGCMs is characterized by robust negative $H_e$ anomalies with an anomalous cyclone (Figs. 2c,e),

and negative streamfunction anomalies (Fig. 2d), suggesting a robust enhancement of the anomalous NPC during the autumn of developing El Niño. In contrast to the fixed interannual SST variability in the AGCMs, the interannual variability of SST anomalies may change in the CGCMs, and the different amplitudes in the change of the anomalous NPC between the AGCMs and CGCMs suggest that the change of the El Niño–related SST anomalies may play a significant role in modulating the change of WNP circulation under global warming.

Two indexes are adopted to quantitatively evaluate the change of the anomalous NPC. Figures 3a and 3b show the absolute change of the $H_e$ index and $\psi$ index during the autumn of developing El Niño, where the $H_e$ index is defined as the regional averaged $H_e$ anomalies within the red box shown in Fig. 2a, and the $\psi$ index is defined as the regional averaged streamfunction anomalies within the green box shown in Fig. 2b. As consistently shown by these two indexes, the anomalous NPC is weakly enhanced in RCP8.5 and robustly enhanced in the AMIP4K and AMIPFuture experiments in the MMM in terms of enhanced negative $H_e$ and streamfunction anomalies over the WNP, and the amplitude of enhancement is stronger in AMIPFuture than in AMIP4K. Based on the $\psi$ index, the MMM of the percentage changes for the intensity of the anomalous NPC are 2.8%, 6.7%, and 14.0% $K^{-1}$ in the RCP8.5, AMIP4K, and AMIPFuture experiments respectively, relative to the intensity of the anomalous NPC in 20C.

Previous studies indicated that the change of the WNP circulation anomalies is largely attributed to ENSO regime shift (Zhang et al. 2011, 2014) in the observation, with the central Pacific El Niño occurring more frequently and eastern Pacific El Niño becoming less common after the 1990s (Lee and McPhaden 2010; Xiang et al. 2013; Zhang et al. 2014). Based on the above qualitative and quantitative results, global warming has a significant modulation on the change of the WNP circulation anomalies. A weakly enhanced anomalous North Pacific cyclone is found during the autumn of developing El Niño in a warmer climate in CGCMs, and suffers intermodel uncertainty. Similar changes appear in AGCMs with increased mean state SST but featuring a strong amplitude of enhancement. As the anomalous NPC is ultimately a Rossby wave response to the positive diabatic heating anomaly over the equatorial central-eastern Pacific, the underlying physical mechanisms controlling the change of the anomalous NPC are explored with the aid of a simple Gill model (Wang and Li 1993) in section 5, and the possible causes for the different amplitude of enhancement between CGCMs and AGCMs are further explored in section 6.

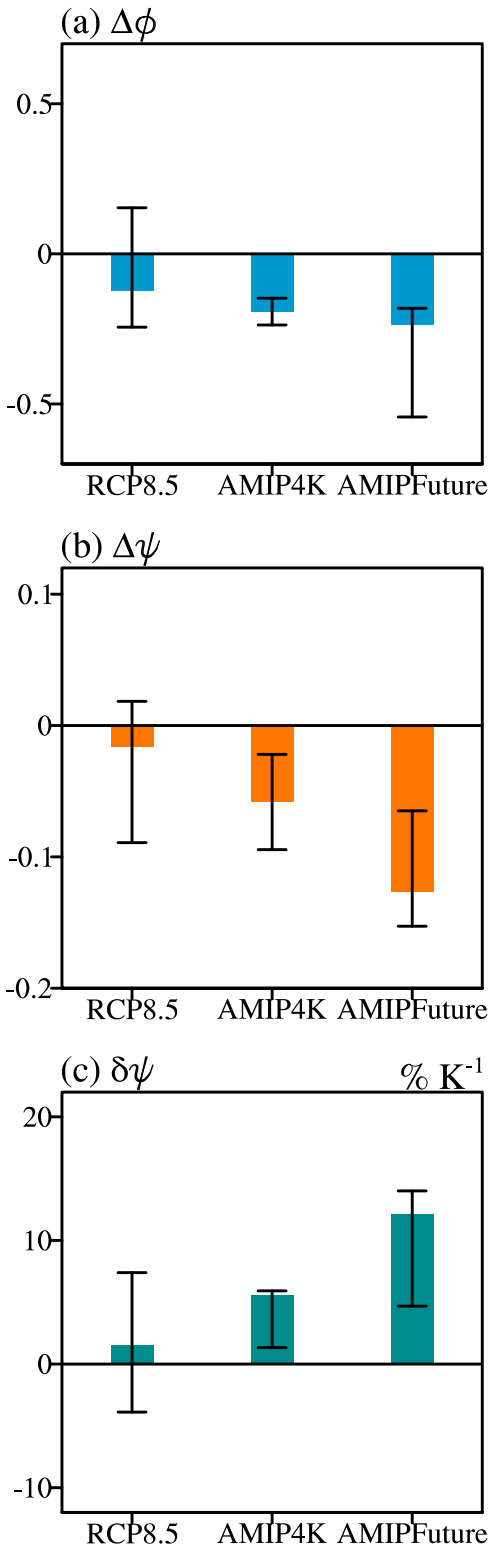


FIG. 3. The absolute change of the (a) $H_e$ index (gpm $K^{-1}$) and (b) $\psi$ index ($10^6$ $m^2$ $s^{-1}$ $K^{-1}$) in the experiments performed by the CGCMs and AGCMs. (c) The percentage change in the intensity of the anomalous NPC based on the $\psi$ index (% $K^{-1}$). The color bar indicates the MMM, and the thin black bar denotes the range between the 30th and 70th percentiles of the individual models.

## 5. Mechanisms for the change of the anomalous North Pacific cyclone in a warmer climate

Most of the previous studies investigated the responses of the atmospheric circulation to global warming by evaluating the behavior of the vertical motion (e.g., He and Li 2019; Held and Soden 2006; Vecchi et al. 2008), and the horizontal component is always overlooked. The traditional method by diagnosing the simplified thermodynamic equation (e.g., Li et al. 2015; Pendergrass and Gerber 2016; He and Li 2019) cannot explain the response of the Gill-type atmospheric anomalies to global warming. The anomalous NPC during the autumn of developing El Niño is stimulated by the positive latent heating anomaly over the equatorial central-eastern Pacific associated with local warm SST anomaly through a Gill-type response (Gill 1980; Wang et al. 2000; Li et al. 2018; Wu et al. 2017b). The atmospheric circulation response to a specified diabatic heating described by the Gill model in an equatorial beta plane with a longwave approximation may be written as

$$\begin{cases} \varepsilon u - \beta y v = -\dfrac{\partial \text{Ø}}{\partial x} \\ \beta y u = -\dfrac{\partial \text{Ø}}{\partial y} \\ \varepsilon \text{Ø} + (1-I)C^2\left(\dfrac{\partial u}{\partial x} + \dfrac{\partial v}{\partial y}\right) = -Q, \end{cases} \tag{1}$$

where $u$, $v$, Ø, and $Q$ represent interannual time scale zonal wind, meridional wind, geopotential, and diabatic heating, respectively; also, $\varepsilon$ is the Rayleigh friction coefficient, $c$ is the first-baroclinic gravity wave speed, $I$ is the heating coefficient, and $\beta$ denotes the equivalent beta [$\beta = \beta_0 + (\partial\overline{\zeta}/\partial y)$]. Based on Eq. (1), the rotational component of atmospheric circulation (designated by streamfunction $\psi$) and its change can be obtained, and the detailed derivation is described in the appendix. Considering a steady-state response at each equilibrium states and using $\delta$ to denote the fractional change between two equilibrium states, the response of the rotational component of atmospheric circulation to global warming is expressed as

$$\delta(\psi) = \delta(Q) - A \times \delta(\overline{\sigma}) + B \times \delta\left(\frac{\partial \overline{\zeta}}{\partial y}\right), \tag{2}$$

where $\psi$ is the streamfunction anomaly calculated from the low-level wind anomaly, and parameters $A$ and $B$ are the functions of atmospheric mean state static stability and meridional gradient of the mean state relative vorticity respectively. The detailed derivations for Eq. (2) are described in the appendix. Given the Rayleigh friction coefficient of 1.0 day$^{-1}$ and characteristic zonal length scale of 5000 km, the parameters $A$ and $B$ can be calculated, and Eq. (2) can be written as

$$\delta(\psi) = \delta(Q) - 0.62 \times \delta(\overline{\sigma}) + 0.1 \times \delta\left(\frac{\partial \overline{\zeta}}{\partial y}\right). \tag{3}$$

Equation (3) shows that the fractional change of the anomalous low-level circulation response to a specified El Niño–forced diabatic heating anomaly under global warming is determined by the fractional change of the diabatic heating anomaly $Q$, mean state static stability $\overline{\sigma}$, and the meridional gradient of the mean state relative vorticity $\partial\overline{\zeta}/\partial y$. To understand the relative contributions from the three factors, the spatial pattern and the magnitude of changes of these three factors are evaluated in Figs. 4 and 5.

As the latent heating anomaly dominates the diabatic heating anomaly over the tropical Pacific associated with ENSO, Figs. 4a–c show the changes of precipitation anomaly over the tropical Pacific. All the experiments performed by the CGCMs and the AGCMs consistently project an enhanced anomalous precipitation over the equatorial central-eastern Pacific. As shown in Fig. 5a, the precipitation anomaly is robustly enhanced by 5.4%, 7.0%, and 16.5% K$^{-1}$ in the RCP8.5, AMIP4K, and AMIPFuture experiments, respectively, consistent with the differentiated magnitudes of enhancement of the anomalous NPC among these three experiments.

As a result of the moist adiabatic adjustment (Knutson and Manabe 1995; Schneider et al. 2010), the upper-tropospheric temperature increases at a higher rate than lower-troposphere temperature (Fig. S4), and the mean state static stability is thus robustly strengthened in a warmer climate (Figs. 4d–f). The amplitudes in the enhancement of the mean state static stability over the tropical Pacific are 3.7%, 4.2%, and 4.5% K$^{-1}$ in the RCP8.5, AMIP4K, and AMIPFuture experiments, respectively, which are close to each other (Fig. 5b). The enhanced mean state static stability could reduce the sensitivity of the anomalous atmospheric circulation to the diabatic heating anomaly (Li et al. 2015; P. Huang et al. 2017; He and Li 2019; He et al. 2019a), acting as a competing role compared to the enhanced diabatic heating anomaly.

Based on the observation, the value of the meridional gradient of the mean state relative vorticity over the near-equatorial WNP dominates the behavior of the anomalous NPC during the El Niño developing phase (Wu et al. 2017b); thus, the near-equatorial WNP (denoted by the black dashed rectangles in Figs. 4g–i) is selected as the key region to evaluate the change of the

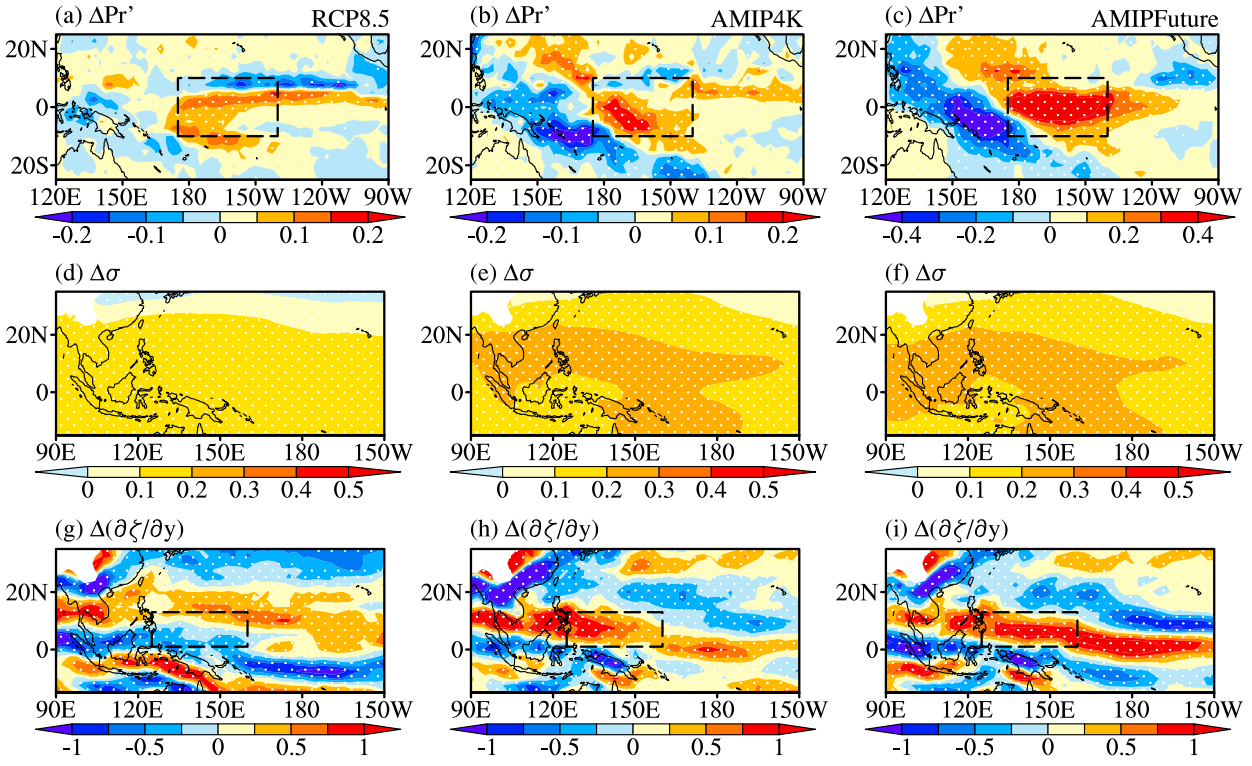


FIG. 4. The projected change (scaled by the tropical mean SST warming) of the precipitation anomaly over the tropical Pacific (mm day$^{-1}$ K$^{-1}$), mean state static stability ($10^{-6}$ m$^2$ s$^{-2}$ Pa$^{-2}$ K$^{-1}$), and the meridional gradient of the mean state relative vorticity (s$^{-2}$ K$^{-1}$) over the WNP in the (left) RCP8.5, (center) AMIP4K, and (right) AMIPFuture experiments. The changes agreeing with at least 70% of the individual models are stippled.

meridional gradient of the mean state relative vorticity. Compared to the 20C, no robust signals are found over the key region in the MMM of CGCMs (Fig. 4g), while the meridional gradient of the mean state relative vorticity is robustly strengthened in the AGCMs (Figs. 4h–i). The change of the meridional gradient of the mean state relative vorticity may result from the change of the climatological cyclone over the SCS and the

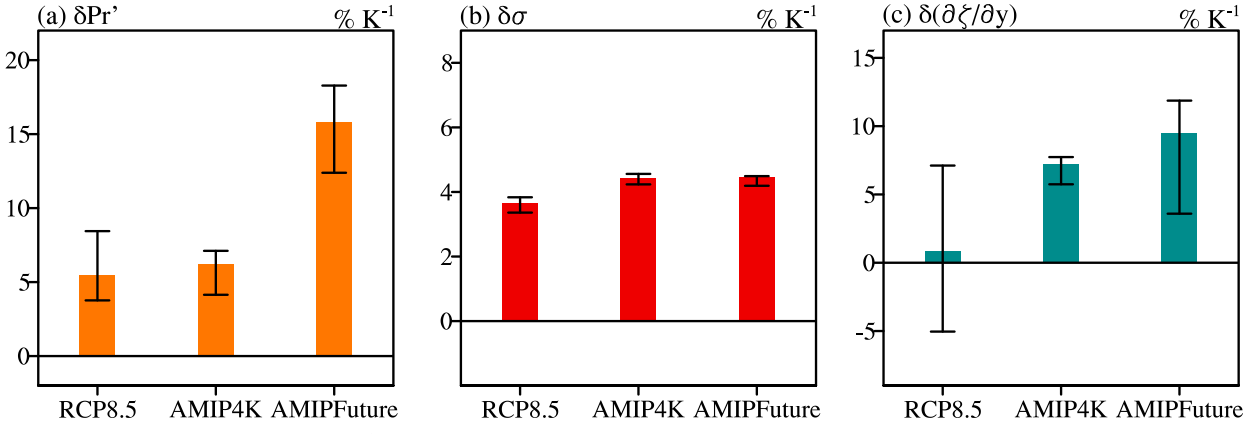


FIG. 5. The percentage change (% K$^{-1}$) of the three key factors in the RCP8.5, AMIP4K, and AMIPFuture experiments. The color bar indicates the MMM, and the thin black bar denotes the range between the 30th and 70th percentiles of the individual models. The three key factors are (a) the precipitation anomaly over the equatorial central-eastern Pacific (10°S–10°N, 170°E–140°W) denoted by the black rectangles in Figs. 4a–c; (b) the mean state static stability over the tropical Pacific (30°S–30°N, 120°E–80°W); and (c) the meridional gradient of the mean state relative vorticity over the near-equatorial WNP (1°–13°N, 125°–160°E) denoted by the black rectangles in Figs. 4g–i.

TABLE 1. The relative contribution (% $K^{-1}$) of the diabatic heating anomaly over the equatorial central-eastern Pacific [$\delta(Q)$], mean state static stability [$-0.62\times\delta(\overline{\sigma})$], and the meridional gradient of the mean state relative vorticity over the near-equatorial WNP [$0.1\times\delta(\partial\overline{\zeta}/\partial y)$] to the fractional change of anomalous NPC [$\delta(\psi)$] based on the MMM. The predicted fractional changes of the anomalous NPC based on the theoretical model [Eq. (3); $\delta(Q)-0.62\times\delta(\overline{\sigma})+0.1\times\delta(\partial\overline{\zeta}/\partial y)$] are shown in the penultimate row, and the CGCM-simulated and AGCM-simulated fractional changes in the intensity of the anomalous NPC [$\delta(\psi)$] are shown in the last row.

| | RCP8.5 | AMIP4K | AMIPFuture |
|---|---|---|---|
| $\delta(Q)$ | 5.4 | 7.0 | 16.5 |
| $-0.62\times\delta(\overline{\sigma})$ | −2.3 | −2.6 | −2.8 |
| $0.1\times\delta(\partial\overline{\zeta}/\partial y)$ | 0.05 | 0.69 | 0.90 |
| $\delta(Q)-0.62\times\delta(\overline{\sigma})+0.1\times\delta(\partial\overline{\zeta}/\partial y)$ | 3.1 | 5.1 | 14.6 |
| $\delta(\psi)$ | 2.8 | 6.7 | 14.0 |

subtropical high over the North Pacific (Fig. S5). Figure 5c evaluates the change in its regional averaged value over the key region. The percentage change of the meridional gradient of the mean state relative vorticity is 0.5%, 6.9%, and 9.2% $K^{-1}$ in the RCP8.5, AMIP4K, and AMIPFuture experiments, respectively. According to Wu et al. (2017b), the enhanced meridional gradient of the mean state relative vorticity favors an enhanced anomalous NPC.

A quantitative evaluation of the three terms in the theoretical model [Eq. (3)] is presented in Table 1. The changes in the intensity of anomalous NPC in terms of the $\psi$ index are 2.8%, 6.7%, and 14.0% $K^{-1}$ for the RCP8.5, AMIP4K, and AMIPFuture experiments, respectively, and the theoretical model predicts a change of 3.1%, 5.1%, and 14.6% $K^{-1}$ under the prescribed changes of El Niño–forced diabatic heating anomaly $Q$, mean state static stability $\overline{\sigma}$, and the meridional gradient of the mean state relative vorticity $\partial\overline{\zeta}/\partial y$ over the near-equatorial WNP for these three experiments. The predicted changes in the intensity of anomalous NPC are close to the values based on the comprehensive models, demonstrating that the theoretical model quantitatively captures the relative contributions of the essential factors responsible for the response of the anomalous NPC to global warming. The quantitative changes of the three terms on the right-hand side of Eq. (3) shown in Table 1 suggest the change of the anomalous NPC is largely determined by the competition between the diabatic heating anomaly and mean state static stability, while the meridional gradient of the mean state relative vorticity has a modest effect.

According to the above diagnoses on the comprehensive model results in the framework of a simple Gill model, the enhanced diabatic heating anomaly makes a much greater contribution to the enhanced anomalous NPC compared with the enhanced meridional gradient of mean state relative vorticity, and it is responsible for the general enhancement of the anomalous NPC. Meanwhile, the amplitudes of enhancement of the mean state static stability are similar in magnitude per degree of warming among the three experiments, and the different amplitudes of enhancement between the CGCMs and AGCMs mainly originate from the different amplitudes of the enhanced diabatic heating anomaly. As the diabatic heating anomaly over the equatorial Pacific is dominated by latent heating anomaly associated with precipitation anomaly, the mechanisms for the amplitudes of change in the precipitation anomaly among the three experiments are explored in the next section.

## 6. Mechanisms for the amplitude of change in the precipitation anomaly over the equatorial Pacific

### *a. The effect of the SST warming pattern*

The difference between the AMIP4K and AMIPFuture experiments originates from the spatial pattern of mean state SST warming. The pattern of mean state SST warming prescribed in the AMIPFuture experiment is characterized by an El Niño–like pattern over the tropical Pacific (Fig. S6a), which is different from a spatially uniform warming of 4 K in the AMIP4K experiment. Figure 6 examines how the SST warming pattern modulates the change of the precipitation anomaly through modulating the mean state precipitation over the equatorial Pacific.

Figure 6a shows the difference in the amplitudes of enhancement of the mean state precipitation between the AMIPFuture and AMIP4K experiments, in comparison with the difference of the mean state SST warming. The enhancement of mean state precipitation is much stronger over the equatorial Pacific in the AMIPFuture experiment than in the AMIP4K experiment, with the largest difference over the equatorial central-eastern Pacific, suggesting that the El Niño–like warming pattern can result in a stronger increase of local mean state precipitation (Xie et al. 2010; Grose et al. 2014). As shown in Figs. 6b–d, the precipitation anomaly over the equatorial central-eastern Pacific has a strong linear relationship with the local mean state precipitation. The high correlations suggest that

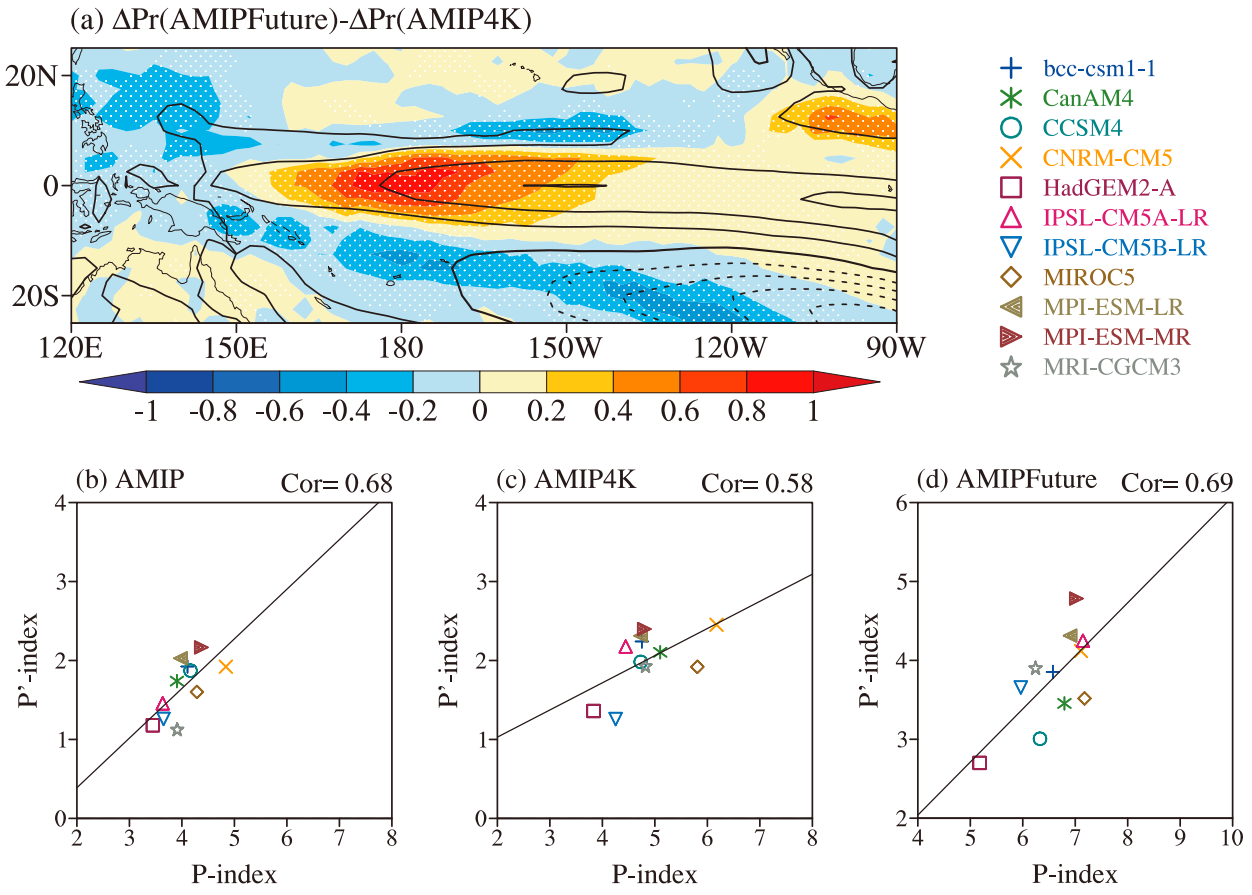


FIG. 6. (a) The difference of the amplitude of enhancement in the mean state precipitation between the AMIPFuture and AMIP4K experiments (shading; mm day$^{-1}$ K$^{-1}$) and the mean state SST warming (contours; K). The contours are from −3.2 to 3.2 K with an interval of 0.4 K, and the negative contours are dashed. The differences in precipitation agreeing in sign with at least 70% of the individual models are stippled. (b)–(d) Scatter diagram for the $P'$ index (mm day$^{-1}$ K$^{-1}$) as a function of the $P$ index (mm day$^{-1}$) in the AMIP, AMIP4K, and AMIPFuture experiments, respectively. The $P'$ index is defined as the regional averaged precipitation anomaly during the autumn of developing El Niño over the equatorial central-eastern Pacific (5°S–5°N, 170°E–140°W), and the $P$ index is defined as the regional averaged mean state precipitation over the equatorial Pacific (5°S–5°N, 150°E–120°W). The intermodel correlation coefficient is marked at the top right for each panel.

the intensity of the precipitation anomaly is largely modulated by the abundance of the current mean state precipitation (He et al. 2017), and a stronger mean state precipitation favors a stronger precipitation anomaly over the equatorial central-eastern Pacific during El Niño. The results indicate that the stronger increase of mean state precipitation under an El Niño–like warming pattern in the AMIPFuture experiment is responsible for the stronger enhancement of precipitation anomaly over the equatorial central-eastern Pacific, and explains why the enhancement of the anomalous NPC is stronger in the AMIPFuture experiment than in the AMIP4K experiment. Those results demonstrate the significant role of the SST warming pattern in modulating the intensity of the atmospheric circulation during El Niño, consistent with Zhou et al. (2014), who emphasized the importance of the SST warming pattern in affecting the PNA teleconnection pattern during El Niño mature winter.

### b. *The effect of the El Niño–related SST anomaly*

Although a similar El Niño–like warming pattern of mean state SST exists in both the RCP8.5 and AMIPFuture experiments (Fig. S6), the amplitude of enhancement in the anomalous NPC is much weaker in the RCP8.5 experiment than in the AMIPFuture experiment. In contrast to the fixed interannual SST variability in the AGCM experiments, the interannual variability of SST anomalies may change in the CGCMs under global warming. The change of the El Niño–related SST anomalies in the MMM of the CGCMs and its possible modulation on the change of the precipitation anomaly over the equatorial Pacific are further investigated respectively.

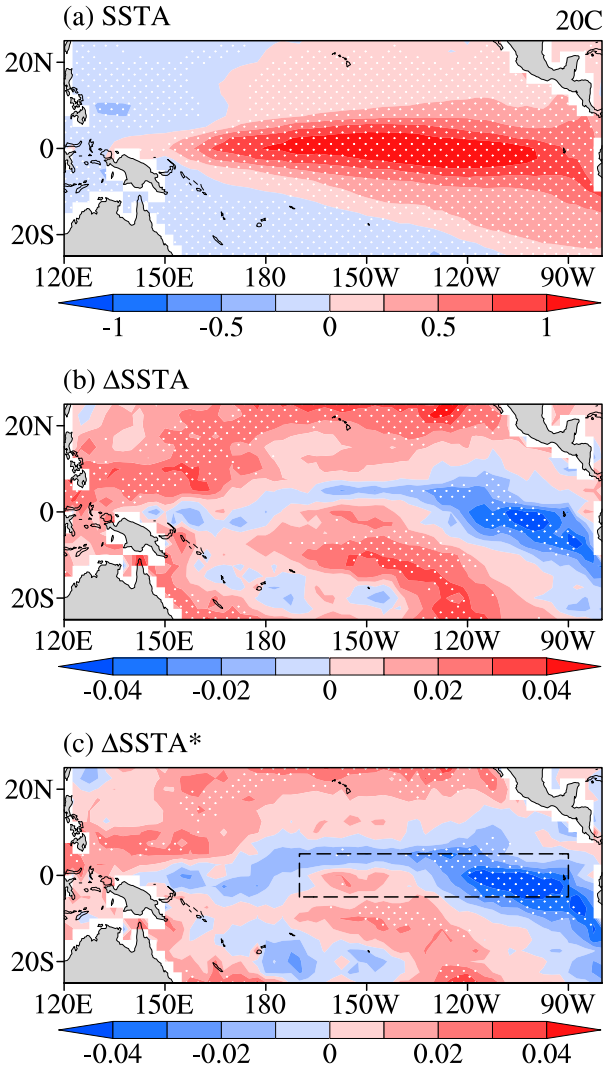


FIG. 7. (a) Regressed SST anomalies (K $K^{-1}$) during the autumn of developing El Niño onto the simultaneous Niño-3.4 index in the Historical experiment. (b) The projected change of the regressed SST anomalies (K $K^{-1}$) in the RCP8.5 experiment relative to the Historical experiment. (c) As in (b), but for the change of the eddy component of SST anomaly (SSTA*), where the SSTA* is defined by removing the simultaneous tropical (20°S–20°N, 120°E–90°W) mean SST anomalies. The changes agreeing with at least 70% of the individual models are stippled. The black dashed rectangle denotes the key region (5°S–5°N, 170°–90°W) selected to define the El Niño pattern index.

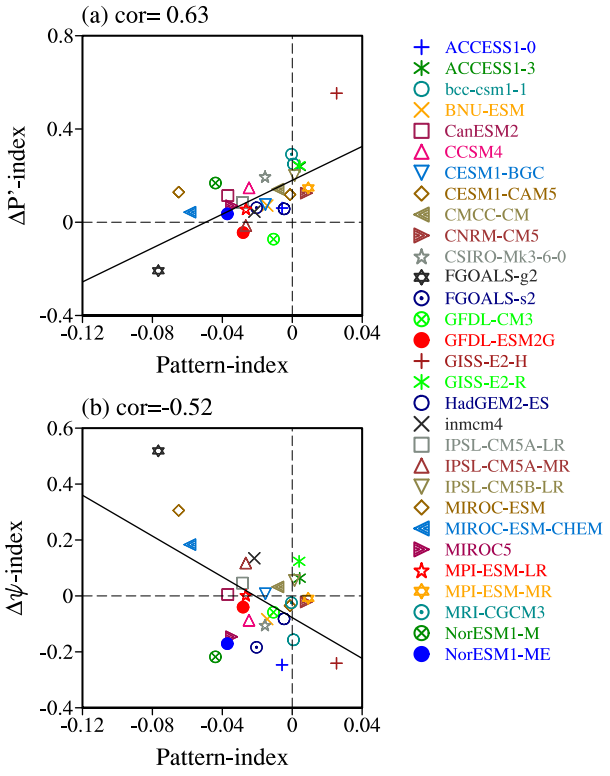


FIG. 8. Scatter diagram for (a) the change of the $\Delta P'$ index (mm $day^{-1}$ $K^{-1}$) and (b) the change of the $\psi$ index ($10^6$ $m^2$ $s^{-1}$ $K^{-1}$) as a function of the change in the El Niño pattern index (K $K^{-1}$). The $\Delta P'$ index is defined as the regional averaged change of the precipitation anomaly over the equatorial central-eastern Pacific (5°S–5°N, 170°E–140°W), and the pattern index is defined as the averaged SSTA* over the box shown in Fig. 7c. The intermodel correlation coefficient is marked in the top left for each panel.

In 20C, warm SST anomalies are seen in the equatorial central-eastern Pacific, with two cold SST anomaly belts on its northern and southern flanks (Fig. 7a). As seen in the change of the El Niño–related SST anomalies in RCP8.5 relative to the Historical experiment (Fig. 7b), warm SST anomalies are seen over the off-equatorial Pacific whereas cold SST anomalies are seen over the equatorial eastern Pacific. Although no robust changes are found over the Niño-3.4 region and large intermodel spread is present in ENSO amplitude change (Collins et al. 2010; Chen et al. 2015; Maher et al. 2018), this pattern of change in SST anomaly may modulate the response of precipitation anomaly since tropical precipitation follows the relatively high SST (Johnson and Xie 2010). After removing mean SST anomalies over the tropical Pacific, the change of the eddy component of SST anomaly (SSTA*, defined by removing the simultaneous tropical mean SST anomalies) suggests a weakened SST anomaly pattern associated with El Niño (Fig. 7c), and it acts to weaken the precipitation anomaly over the equatorial Pacific during the autumn of developing El Niño. The intermodel relationship between the changes in the precipitation anomaly over the equatorial central-eastern Pacific as a function of the change in the El Niño pattern index (also simply pattern index or $P$ index) is shown in Fig. 8a, where the El Niño pattern index is defined as regional averaged SSTA* over the equatorial central-eastern Pacific (5°S–5°N, 170°–90°W). The robustly

weakened El Niño pattern index during the autumn of developing El Niño in a warmer climate is seen in 23 of 30 CGCMs (Fig. 8a), and these two quantities have an intermodel correlation of 0.63. These evidences indicate that the change of the SST anomaly pattern does have an impact on the intensity of the precipitation anomaly over the equatorial central-eastern Pacific, and the weakened El Niño–related SST anomaly pattern reduces the enhancement of the precipitation anomaly. Figure 8b further investigates the relationship between the change of the El Niño pattern and the intensity of the anomalous NPC. The linear correlation between the El Niño pattern index and the change of the $\psi$ index is $-0.52$, suggesting the weakened El Niño–SST anomaly pattern does weaken the anomalous NPC by weakening the enhancement of the precipitation anomaly over the equatorial central-eastern Pacific.

The above analyses demonstrate that the weakened El Niño–related SST anomaly pattern is responsible for the weaker enhancement of the anomalous NPC in the RCP8.5 experiment than in the AMIPFuture experiment. The weakened El Niño–SST anomaly partially offsets the enhancement of the precipitation anomaly, and weakens the enhancement of the anomalous NPC. Those results suggest that the change of the SST anomaly associated with El Niño also plays a nonnegligible role in modulating the response of the atmospheric circulation anomalies during El Niño to global warming (Jiang et al. 2018).

## 7. Conclusions and discussion

### a. Conclusions

El Niño stimulates an anomalous cyclone over the WNP during its developing phase, and the anomalous North Pacific cyclone (NPC) has a profound impact on the East Asian climate variability. In the current study, using the outputs from 30 CGCMs and 11 AGCMs, the impact of global warming on the anomalous NPC during the autumn of developing El Niño is investigated, and a theoretical framework based on Gill model is adopted to understand the underlying mechanisms. The major findings are summarized as follows.

1) As projected by the CGCMs through the comparison between the RCP8.5 and Historical experiments, the anomalous NPC during the autumn of developing El Niño is weakly strengthened by $2.8\%\,K^{-1}$ in the MMM and suffers intermodel uncertainty. Based on the AMIP4K and AMIPFuture experiments compared with the AMIP experiment when keeping the El Niño–related SST anomaly unchanged, the pattern of change in the atmospheric circulation anomalies over the WNP under mean state SST warming shares a similar pattern of change with the CGCMs, but the amplitude of the enhancement of the anomalous NPC is stronger.
2) A theoretical framework developed based on a simple Gill model well explains the change of the anomalous NPC under global warming. Based on the theoretical model, a diabatic heating anomaly over the equatorial central-eastern Pacific, mean state static stability, and the meridional gradient of the mean state relative vorticity over the near-equatorial WNP are identified to be the three key factors controlling the response of the anomalous NPC to global warming. A quantitative diagnosis of the CGCM and AGCM experiments suggests that the change of the anomalous NPC is largely determined by the competition between the diabatic heating anomaly and mean state static stability, whereas the meridional gradient of the mean state relative vorticity has only a modest effect.
3) The amplitude of enhancement of the anomalous NPC per degree of mean state warming is stronger in AGCMs than in CGCMs, and stronger in the AMIPFuture experiment than in the AMIP4K experiment for the AGCMs. The differentiated amplitudes of enhancement of the anomalous NPC originate from the change in latent heating anomaly over the equatorial central-eastern Pacific, which are modulated by the change of the mean state SST warming pattern and the El Niño–related SST anomaly. Compared with a uniform warming in AMIP4K experiment, the El Niño–like mean state SST warming pattern strengthens the enhancement of the precipitation anomaly through strengthening the mean state precipitation in the AMIPFuture experiment, and favors a much stronger enhancement of anomalous NPC. However, the weakened El Niño–related SST anomaly due to air–sea coupling in CGCMs partially offsets the enhanced precipitation anomaly over equatorial Pacific, which explains why the magnitude of enhancement of anomalous NPC is weaker in CGCMs than in AGCMs.

### b. Discussion

The change of the atmospheric anomalies is simply scaled by the tropical mean SST warming in the above analyses, and the possible nonlinear dependence on the amplitude of the mean SST warming is further investigated. In total 31 periods (i.e., 2040–69, 2041–70, 2042–71, . . . , 2070–99) from the RCP8.5 experiment are selected and compared to the baseline period of 1950–99 in the Historical experiment, and the percentage

changes in the intensity of the anomalous NPC as a function of tropical mean SST warming for these 31 periods are shown in Fig. 9. The amplitude of tropical mean SST warming from the middle to the late twenty-first century ranges approximately from 1.6 to 3 K, and the amplitude of the enhancement in the intensity of the anomalous NPC increases with the mean SST warming. The linear correlation between the tropical mean SST warming and the percentage change of the intensity in the anomalous NPC is 0.76, which is significant at the 99% confidence level. This relationship is also examined in a lower-emission scenario (RCP4.5) with smaller mean SST increase (Fig. S7). In the low-emission scenario, the amplitude of the enhancement in the intensity of the anomalous NPC still increases with the mean SST warming, and the linear correlation between them is 0.62 (significant at 99% confidence level). The high linear correlations suggest that the response of the intensity of the anomalous NPC to the tropical mean SST warming is generally linear, at least within the warming amplitude we focus on. A wider range of mean state warming (or cooling) is required to identify the possible nonlinear response of anomalous NPC to mean state climate change, which should range from the extremely cold (at least dozens of degrees of cooling) to the extremely warm (at least dozens of degrees of warming) climates as advised by previous studies (Schneider et al. 2010; Byrne and O'Gorman 2013; Levine and Boos 2016; Wills and Schneider 2016).

The simulated anomalous NPC in 20C is not exactly the same between CGCMs and AGCMs. Based on the streamfunction anomalies in the MMM, the intensity of the anomalous NPC (evaluated over 5°–30°N, 135°E–150°W) is $-1.34 \times 10^6$ and $-1.22 \times 10^6\,m^2\,s^{-1}$ simulated by the AMIP experiment and Historical experiment, respectively. The intensity of the anomalous NPC in the AMIP experiment is comparable to the Historical experiment, but it is stronger in the AMIP experiment than the Historical experiment by 9.8%, suggesting a slight overestimation of the atmospheric response to SST forcing in AGCMs. However, it is not clear about the possible impact of the bias in 20C simulation on the projected future change, as the intermodel correlation between the simulated intensity of the anomalous NPC in 20C and its change in 21C is only 0.22 among the CGCMs. Future study is needed to address the possible impact of the 20C simulation on the projection of future climate change.

The air–sea coupling in the CGCMs tend to weaken the El Niño–related SST anomaly pattern, which suppresses the enhancement of the positive precipitation anomaly over the equatorial Pacific and reduces the enhancement of the anomalous NPC. The weakened El Niño–related SST anomaly may be due to the response of tropical clouds to global warming (Bony et al. 2004; Bony and Dufresne 2005; Bellomo et al. 2015), which is associated with the negative heat fluxes such as shortwave radiation and latent heat flux and is worthy of further investigation.

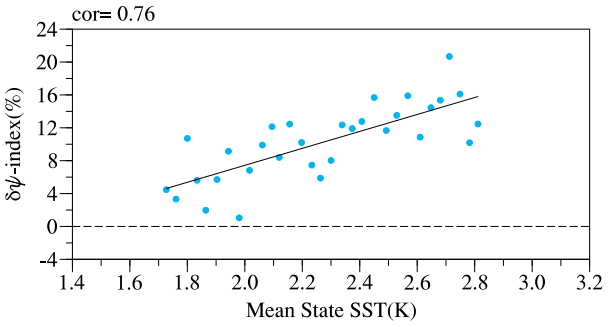


FIG. 9. Scatter diagram for the percentage change of the $\psi$ index (%) as a function of the tropical mean SST warming (K). The 1950–99 period in the Historical experiment is adopted as the baseline period, 31 periods (i.e., 2040–69, 2041–70, 2042–71, . . . , 2070–99) from RCP8.5 experiment are selected and compared to the baseline period, and the percentage change in the intensity of the anomalous NPC is obtained in each warming period. The correlation coefficient between the percentage change of the $\psi$ index and the tropical mean SST warming is marked in the top left of the panel.

As suggested by previous studies, the anomalous NPC is the key bridge for the formation and maintenance of the anomalous western North Pacific anticyclone (WNPAC; Li et al. 2018; Wu et al. 2017b). The anomalous WNPAC usually forms in the developing autumn of El Niño, is fully developed during the mature winter of El Niño, and maintains throughout the El Niño decaying phase, which is an important circulation system directly conveying ENSO's impact on East Asian climate. As shown in Fig. 2, the anomalous anticyclone over the South China Sea shows a complicated change pattern under global warming compared to the anomalous NPC, which may result from multiple processes such as local atmosphere–ocean interaction (Wang et al. 2000) or moist enthalpy advection/Rossby wave modulation (Wu et al. 2017a,b). Previous studies have suggested a weakened anomalous WNPAC during El Niño decaying summer (Jiang et al. 2018; He et al. 2019b) in a warmer climate, and the response of the anomalous WNPAC during other El Niño stages to global warming still remains unknown and deserves further study.

*Acknowledgments.* The authors wish to acknowledge all the modeling groups for providing the model outputs. The authors are also grateful to Dr. Jong-Seong Kug and two anonymous reviewers for helpful comments that significantly improved this article. This work is jointly supported by National Natural Science Foundation of China (41630423 and 41875081), China National Key R&D Program (2017YFA0603802 and 2017YFA0604601), NOAA NA18OAR4310298, and NSF AGS-1643297.

This is SOEST contribution number 10877, IPRC contribution number 1420, and ESMC number 295.

## APPENDIX

### A Theoretical Framework for Understanding the Gill-Type Atmospheric Anomalies' Response to Global Warming

Following Wang and Li (1993), atmospheric circulation response to a specified diabatic heating described by the Gill model (Gill 1980) in an equatorial beta plane with a longwave approximation can be written as

$$\begin{cases} \varepsilon u - \beta y v = -\dfrac{\partial \text{Ø}}{\partial x} \\ \beta y u = -\dfrac{\partial \text{Ø}}{\partial y} \\ \varepsilon \text{Ø} + (1-I)C^2\left(\dfrac{\partial u}{\partial x} + \dfrac{\partial v}{\partial y}\right) = -Q, \end{cases} \tag{A1}$$

where $u, v, \text{Ø}$, and $Q$ denote interannual time scale zonal wind, meridional wind, geopotential, and diabatic heating, respectively. Also, $c$ is the first-baroclinic gravity wave speed, $\varepsilon$ is the Rayleigh friction coefficient, $I$ is the heating coefficient, and $\beta$ denotes the equivalent beta, which is written as

$$\beta = \beta_0 + \frac{\partial \overline{\zeta}}{\partial y}, \tag{A2}$$

where $\beta_0$ is the meridional gradient of the Coriolis parameter and $\overline{\zeta}$ denotes the mean state relative vorticity. According to the momentum equation, $u$ and $v$ can be transformed into a function of Ø:

$$\begin{cases} u = -\dfrac{1}{\beta y}\dfrac{\partial \text{Ø}}{\partial y} \\ v = -\dfrac{1}{\beta y}\dfrac{\partial \text{Ø}}{\partial x} - \dfrac{\varepsilon}{\beta^2 y^2}\dfrac{\partial \text{Ø}}{\partial y}. \end{cases} \tag{A3}$$

Let $L_X$ and $L_Y$ represent characteristic zonal and meridional length scales, respectively, and $L_Y$ is equal to the radius of Rossby deformation ($L_Y = \sqrt{C/\beta}$). The thermodynamic equation in Eq. (A1) may then be written as

$$\text{Ø} = \frac{L_X}{(1-I)C - (4-3I)\varepsilon L_X} Q. \tag{A4}$$

Taking the logarithm and applying total differentiation on both sides of Eq. (A4), one may obtain

$$\frac{d\text{Ø}}{\text{Ø}} = \frac{dQ}{Q} - \frac{(1-I)C}{(1-I)C - (4-3I)\varepsilon L_X}\frac{dC}{C}, \tag{A5}$$

where $d$ denotes the change between two equilibrium states.

The rotational component of atmospheric circulation (designated by streamfunction $\psi$) and its change can be obtained based on Eq. (A3). Combining Eqs. (A3) and (A5), the fractional change of the rotational component of atmospheric circulation can be expressed as

$$\begin{aligned} \frac{d\psi}{\psi} = \frac{d\text{Ø}}{\text{Ø}} &+ \frac{L_X^2\beta - \varepsilon L_X - \dfrac{C}{2}}{C + 2\beta L_X^2 + \varepsilon L_X}\frac{d\beta}{\beta} \\ &- \frac{C + 3(2L_X^2\beta + \varepsilon L_X)}{2(C + 2L_X^2\beta + \varepsilon L_X)}\frac{dC}{C}. \end{aligned} \tag{A6}$$

Based on Eq. (A2), the fractional change of the equivalent beta can be transformed into the function of $\partial\overline{\zeta}/\partial y$:

$$\frac{d\beta}{\beta} = \frac{\dfrac{\partial \overline{\zeta}}{\partial y}}{\beta_0 + \dfrac{\partial \overline{\zeta}}{\partial y}}\frac{d\left(\dfrac{\partial \overline{\zeta}}{\partial y}\right)}{\dfrac{\partial \overline{\zeta}}{\partial y}}, \tag{A7}$$

and the relationship between the gravity wave speed $c$ and the static stability $\overline{\sigma}$ is

$$C^2 = \frac{1}{2}\overline{\sigma}\Delta P^2, \tag{A8}$$

where $\overline{\sigma}$ is the mean state static stability at middle troposphere, and $\Delta P$ denotes the half depth of the free troposphere, which equals 400 hPa.

Combining Eqs. (A5)–(A8), one may finally derive the following relation:

$$\frac{d\psi}{\psi} = \frac{dQ}{Q} - A\frac{d\overline{\sigma}}{\overline{\sigma}} + B\frac{d\left(\dfrac{\partial \overline{\zeta}}{\partial y}\right)}{\dfrac{\partial \overline{\zeta}}{\partial y}}, \tag{A9}$$

where $A$ and $B$ are

$$\begin{cases} A = \dfrac{1}{2}\left[\dfrac{C + 3(2L_X^2\beta + \varepsilon L_X)}{2(C + 2L_X^2\beta + \varepsilon L_X)} - \dfrac{(1-I)C}{(4-3I)\varepsilon L_X - (1-I)C}\right] \\ B = \dfrac{L_X^2\beta - \varepsilon L_X - \dfrac{C}{2}}{C + 2\beta L_X^2 + \varepsilon L_X}\dfrac{\dfrac{\partial \overline{\zeta}}{\partial y}}{\beta_0 + \dfrac{\partial \overline{\zeta}}{\partial y}}. \end{cases}$$

Equation (A9) suggests that the fractional change of the interannual time scale atmospheric circulation is

determined by the fractional change of the diabatic heating, the fractional change of the mean static stability weighted by a parameter $A$, and the fractional change of meridional gradient of the mean state relative vorticity weighted by a parameter $B$.

The Rayleigh friction coefficient and characteristic zonal length scale are given as $1.0\,\text{day}^{-1}$ and 5000 km, respectively, and the values of other coefficients are listed as follows:

$$\begin{cases} \overline{\sigma} = 6.5\times10^{-6}\,\text{m}^2\,\text{s}^{-2}\,\text{Pa}^{-2} \\ \beta_0 = 2.0\times10^{-11}\,\text{s}^{-2} \\ \dfrac{\partial\overline{\zeta}}{\partial y} = 7.0\times10^{-12}\,\text{s}^{-2} \\ C = \sqrt{\dfrac{\overline{\sigma}\Delta p^2}{2}} = 72.1\,\text{m}\,\text{s}^{-1} \\ \beta = \beta_0 + \dfrac{\partial\overline{\zeta}}{\partial y} = 2.7\times10^{-11}\,\text{s}^{-2}. \end{cases}$$

Letting the symbol $\delta$ denote the fractional change of a variable, finally Eq. (A9) can be written as

$$\delta(\psi) = \delta(Q) - 0.62\times\delta(\overline{\sigma}) + 0.1\times\delta\left(\frac{\partial\overline{\zeta}}{\partial y}\right). \qquad \text{(A10)}$$

## REFERENCES


Adler, R. F., and Coauthors, 2003: The version-2 Global Precipitation Climatology Project (GPCP) monthly precipitation analysis (1979–present). *J. Hydrometeor.*, **4**, 1147–1167, https://doi.org/10.1175/1525-7541(2003)004<1147:TVGPCP>2.0.CO;2.

Alexander, M. A., I. Bladé, M. Newman, J. R. Lanzante, N.-C. Lau, and J. D. Scott, 2002: The atmospheric bridge: The influence of ENSO teleconnections on air–sea interaction over the global oceans. *J. Climate*, **15**, 2205–2231, https://doi.org/10.1175/1520-0442(2002)015<2205:TABTIO>2.0.CO;2.

Bellomo, K., A. C. Clement, T. Mauritsen, G. Rädel, and B. Stevens, 2015: The influence of cloud feedbacks on equatorial Atlantic variability. *J. Climate*, **28**, 2725–2744, https://doi.org/10.1175/JCLI-D-14-00495.1.

Bony, S., and J. L. Dufresne, 2005: Marine boundary layer clouds at the heart of tropical cloud feedback uncertainties in climate models. *Geophys. Res. Lett.*, **32**, L20806, https://doi.org/10.1029/2005GL023851.

——, ——, H. Le Treut, J.-J. Morcrette, and C. Senior, 2004: On dynamic and thermodynamic components of cloud changes. *Climate Dyn.*, **22**, 71–86, https://doi.org/10.1007/s00382-003-0369-6.

——, M. Webb, C. Bretherton, S. Klein, P. Siebesma, G. Tselioudis, and M. Zhang, 2011: CFMIP: Towards a better evaluation and understanding of clouds and cloud feedbacks in CMIP5 models. *CLIVAR Exchanges*, No. 56, International CLIVAR Project Office, Southampton, United Kingdom, 20–22.

Byrne, M. P., and P. A. O'Gorman, 2013: Land–ocean warming contrast over a wide range of climates: Convective quasi-equilibrium theory and idealized simulations. *J. Climate*, **26**, 4000–4016, https://doi.org/10.1175/JCLI-D-12-00262.1.

Cai, W., and Coauthors, 2014: Increasing frequency of extreme El Niño events due to greenhouse warming. *Nat. Climate Change*, **4**, 111–116, https://doi.org/10.1038/nclimate2100.

Chen, L., T. Li, and Y. Yu, 2015: Causes of strengthening and weakening of ENSO amplitude under global warming in four CMIP5 models. *J. Climate*, **28**, 3250–3274, https://doi.org/10.1175/JCLI-D-14-00439.1.

Chen, T.-C., S.-P. Weng, N. Yamazaki, and S. Kiehne, 1998: Interannual variation in the tropical cyclone formation over the western North Pacific. *Mon. Wea. Rev.*, **126**, 1080–1090, https://doi.org/10.1175/1520-0493(1998)126<1080:IVITTC>2.0.CO;2.

Chiang, J. C., and A. H. Sobel, 2002: Tropical tropospheric temperature variations caused by ENSO and their influence on the remote tropical climate. *J. Climate*, **15**, 2616–2631, https://doi.org/10.1175/1520-0442(2002)015<2616:TTTVCB>2.0.CO;2.

Collins, M., and Coauthors, 2010: The impact of global warming on the tropical Pacific Ocean and El Niño. *Nat. Geosci.*, **3**, 391–397, https://doi.org/10.1038/ngeo868.

Deser, C., A. Phillips, V. Bourdette, and H. Teng, 2012: Uncertainty in climate change projections: The role of internal variability. *Climate Dyn.*, **38**, 527–546, https://doi.org/10.1007/s00382-010-0977-x.

Gill, A. E., 1980: Some simple solutions for heat-induced tropical circulation. *Quart. J. Roy. Meteor. Soc.*, **106**, 447–462, https://doi.org/10.1002/qj.49710644905.

Gleckler, P. J., K. E. Taylor, and C. Doutriaux, 2008: Performance metrics for climate models. *J. Geophys. Res.*, **113**, D06104, https://doi.org/10.1029/2007JD008972.

Grose, M. R., J. Bhend, S. Narsey, A. Sen Gupta, and J. R. Brown, 2014: Can we constrain CMIP5 rainfall projections in the tropical Pacific based on surface warming patterns? *J. Climate*, **27**, 9123–9138, https://doi.org/10.1175/JCLI-D-14-00190.1.

He, C., and T. Li, 2019: Does global warming amplify interannual climate variability? *Climate Dyn.*, **52**, 2667–2684, https://doi.org/10.1007/S00382-018-4286-0.

——, A. Lin, D. Gu, C. Li, and B. Zheng, 2017: Formation mechanism for the amplitude of interannual climate variability in subtropical Northern Hemisphere: Relative contributions from the zonal asymmetric mean state and the interannual variability of SST. *Climate Dyn.*, **48**, 697–705, https://doi.org/10.1007/s00382-016-3105-8.

——, ——, ——, ——, ——, B. Wu, and T. Zhou, 2018: Using eddy geopotential height to measure the western North Pacific subtropical high in a warming climate. *Theor. Appl. Climatol.*, **131**, 681–691, https://doi.org/10.1007/s00704-016-2001-9.

——, Y. Wang, and T. Li, 2019a: Weakened impact of the developing El Niño on tropical Indian Ocean climate variability under global warming. *J. Climate*, **32**, 7265–7279, https://doi.org/10.1175/JCLI-D-19-0165.1.

——, T. Zhou, and T. Li, 2019b: Weakened anomalous western North Pacific anticyclone during El Niño–decaying summer under a warmer climate: Dominant role of the weakened impact of the tropical Indian Ocean on the atmosphere. *J. Climate*, **32**, 213–230, https://doi.org/10.1175/JCLI-D-18-0033.1.

——, R. Liu, X. Wang, S. C. Liu, T. Zhou, and W. Liao, 2019c: How does El Niño–Southern Oscillation modulate the interannual variability of winter haze days over eastern China? *Sci. Total Environ.*, **651**, 1892–1902, https://doi.org/10.1016/j.scitotenv.2018.10.100.

Held, I. M., and B. J. Soden, 2006: Robust responses of the hydrological cycle to global warming. *J. Climate*, **19**, 5686–5699, https://doi.org/10.1175/JCLI3990.1.

Hoskins, B. J., and D. J. Karoly, 1981: The steady linear response of a spherical atmosphere to thermal and orographic forcing. *J. Atmos. Sci.*, **38**, 1179–1196, https://doi.org/10.1175/1520-0469(1981)038<1179:TSLROA>2.0.CO;2.

Huang, B., and Coauthors, 2017: Extended Reconstructed Sea Surface Temperature, version 5 (ERSSTv5): Upgrades, validations, and intercomparisons. *J. Climate*, **30**, 8179–8205, https://doi.org/10.1175/JCLI-D-16-0836.1.

Huang, P., D. Chen, and J. Ying, 2017: Weakening of the tropical atmospheric circulation response to local sea surface temperature anomalies under global warming. *J. Climate*, **30**, 8149–8158, https://doi.org/10.1175/JCLI-D-17-0171.1.

Jiang, L., and T. Li, 2018: Why rainfall response to El Niño over Maritime Continent is weaker and non-uniform in boreal winter than in boreal summer. *Climate Dyn.*, **51**, 1465–1483, https://doi.org/10.1007/s00382-017-3965-6.

Jiang, W., G. Huang, P. Huang, and K. Hu, 2018: Weakening of northwest Pacific anticyclone anomalies during post–El Niño summers under global warming. *J. Climate*, **31**, 3539–3555, https://doi.org/10.1175/JCLI-D-17-0613.1.

Johnson, N. C., and S.-P. Xie, 2010: Changes in the sea surface temperature threshold for tropical convection. *Nat. Geosci.*, **3**, 842–845, https://doi.org/10.1038/ngeo1008.

Kalnay, E., and Coauthors, 1996: The NCEP/NCAR 40-Year Reanalysis Project. *Bull. Amer. Meteor. Soc.*, **77**, 437–471, https://doi.org/10.1175/1520-0477(1996)077<0437:TNYRP>2.0.CO;2.

Keil, A., M. Zeller, A. Wida, B. Sanim, and R. Birner, 2008: What determines farmers' resilience towards ENSO-related drought? An empirical assessment in Central Sulawesi, Indonesia. *Climatic Change*, **86**, 291–307, https://doi.org/10.1007/s10584-007-9326-4.

Knutson, T. R., and S. Manabe, 1995: Time-mean response over the tropical Pacific to increased $CO_2$ in a coupled ocean–atmosphere model. *J. Climate*, **8**, 2181–2199, https://doi.org/10.1175/1520-0442(1995)008<2181:TMROTT>2.0.CO;2.

Kug, J.-S., S.-I. An, Y.-G. Ham, and I.-S. Kang, 2010: Changes in El Niño and La Niña teleconnections over North Pacific–America in the global warming simulations. *Theor. Appl. Climatol.*, **100**, 275–282, https://doi.org/10.1007/s00704-009-0183-0.

Lee, T., and M. J. McPhaden, 2010: Increasing intensity of El Niño in the central-equatorial Pacific. *Geophys. Res. Lett.*, **37**, L14603, https://doi.org/10.1029/2010GL044007.

Levine, X. J., and W. R. Boos, 2016: A mechanism for the response of the zonally asymmetric subtropical hydrologic cycle to global warming. *J. Climate*, **29**, 7851–7867, https://doi.org/10.1175/JCLI-D-15-0826.1.

Li, S., Z. Han, and H. Chen, 2017: A comparison of the effects of interannual Arctic sea ice loss and ENSO on winter haze days: Observational analyses and AGCM simulations. *J. Meteor. Res.*, **31**, 820–833, https://doi.org/10.1007/s13351-017-7017-2.

Li, T., L. Zhang, and H. Murakami, 2015: Strengthening of the Walker circulation under global warming in an aqua-planet general circulation model simulation. *Adv. Atmos. Sci.*, **32**, 1473–1480, https://doi.org/10.1007/s00376-015-5033-7.

——, B. Wang, B. Wu, T. Zhou, C.-P. Chang, and R. Zhang, 2018: Theories on formation of an anomalous anticyclone in western North Pacific during El Niño: A review. *J. Meteor. Res.*, **31**, 987–1006, https://doi.org/10.1007/s13351-017-7147-6.

Maher, N., D. Matei, S. Milinski, and J. Marotzke, 2018: ENSO change in climate projections: Forced response or internal variability? *Geophys. Res. Lett.*, **45**, 11 390–11 398, https://doi.org/10.1029/2018GL079764.

Naughten, K. A., K. J. Meissner, B. K. Galton-Fenzi, M. H. England, R. Timmermann, and H. H. Hellmer, 2018: Future projections of Antarctic ice shelf melting based on CMIP5 scenarios. *J. Climate*, **31**, 5243–5261, https://doi.org/10.1175/JCLI-D-17-0854.1.

Pendergrass, A. G., and E. P. Gerber, 2016: The rain is askew: Two idealized models relating vertical velocity and precipitation distributions in a warming world. *J. Climate*, **29**, 6445–6462, https://doi.org/10.1175/JCLI-D-16-0097.1.

Perry, S. J., and Coauthors, 2017: Future changes to El Niño–Southern Oscillation temperature and precipitation teleconnections. *Geophys. Res. Lett.*, **44**, 10 608–10 616, https://doi.org/10.1002/2017GL074509.

Power, S. B., F. Delage, R. Colman, and A. Moise, 2012: Consensus on twenty-first-century rainfall projections in climate models more widespread than previously thought. *J. Climate*, **25**, 3792–3809, https://doi.org/10.1175/JCLI-D-11-00354.1.

——, ——, C. Chung, G. Kociuba, and K. Keay, 2013: Robust twenty-first-century projections of El Niño and related precipitation variability. *Nature*, **502**, 541–545, https://doi.org/10.1038/nature12580.

Rasmusson, E. M., and T. H. Carpenter, 1982: Variations in tropical sea surface temperature and surface wind fields associated with the Southern Oscillation/El Niño. *Mon. Wea. Rev.*, **110**, 354–384, https://doi.org/10.1175/1520-0493(1982)110<0354:VITSST>2.0.CO;2.

Schneider, T., P. A. O'Gorman, and X. J. Levine, 2010: Water vapor and the dynamics of climate changes. *Rev. Geophys.*, **48**, RG3001, https://doi.org/10.1029/2009RG000302.

Taylor, K. E., R. J. Stouffer, and G. A. Meehl, 2012: An overview of CMIP5 and the experiment design. *Bull. Amer. Meteor. Soc.*, **93**, 485–498, https://doi.org/10.1175/BAMS-D-11-00094.1.

Trenberth, K. E., G. W. Branstator, D. Karoly, A. Kumar, N.-C. Lau, and C. Ropelewski, 1998: Progress during TOGA in understanding and modeling global teleconnections associated with tropical sea surface temperatures. *J. Geophys. Res.*, **103**, 14 291–14 324, https://doi.org/10.1029/97JC01444.

van Vuuren, D. P., and Coauthors, 2011: The representative concentration pathways: An overview. *Climatic Change*, **109**, 5–31, https://doi.org/10.1007/s10584-011-0148-z.

Vecchi, G. A., A. Clement, and B. J. Soden, 2008: Examining the tropical Pacific's response to global warming. *Eos, Trans. Amer. Geophys. Union*, **89**, 81–83, https://doi.org/10.1029/2008EO090002.

Wang, B., and T. Li, 1993: A simple tropical atmosphere model of relevance to short-term climate variations. *J. Atmos. Sci.*, **50**, 260–284, https://doi.org/10.1175/1520-0469(1993)050<0260:ASTAMO>2.0.CO;2.

——, and J. C. L. Chan, 2002: How strong ENSO events affect tropical storm activity over the western North Pacific. *J. Climate*, **15**, 1643–1658, https://doi.org/10.1175/1520-0442(2002)015<1643:HSEEAT>2.0.CO;2.

——, R. Wu, and X. Fu, 2000: Pacific–East Asian teleconnection: How does ENSO affect East Asian climate? *J. Climate*, **13**, 1517–1536, https://doi.org/10.1175/1520-0442(2000)013<1517:PEATHD>2.0.CO;2.

——, ——, and T. Li, 2003: Atmosphere–warm ocean interaction and its impacts on Asian–Australian monsoon variation. *J. Climate*, **16**, 1195–1211, https://doi.org/10.1175/1520-0442(2003)16<1195:AOIAII>2.0.CO;2.

Webster, P. J., and S. Yang, 1992: Monsoon and ENSO: Selectively interactive systems. *Quart. J. Roy. Meteor. Soc.*, **118**, 877–926, https://doi.org/10.1002/qj.49711850705.

——, V. O. Magaña, T. Palmer, J. Shukla, R. Tomas, M. Yanai, and T. Yasunari, 1998: Monsoons: Processes, predictability, and the prospects for prediction. *J. Geophys. Res.*, **103**, 14 451–14 510, https://doi.org/10.1029/97JC02719.

Wills, R. C., and T. Schneider, 2016: How stationary eddies shape changes in the hydrological cycle: Zonally asymmetric experiments in an idealized GCM. *J. Climate*, **29**, 3161–3179, https://doi.org/10.1175/JCLI-D-15-0781.1.

Wu, B., T. Zhou, and T. Li, 2017a: Atmospheric dynamic and thermodynamic processes driving the western North Pacific anomalous anticyclone during El Niño. Part I: Maintenance mechanisms. *J. Climate*, **30**, 9621–9635, https://doi.org/10.1175/JCLI-D-16-0489.1.

——, ——, and ——, 2017b: Atmospheric dynamic and thermodynamic processes driving the western North Pacific anomalous anticyclone during El Niño. Part II: Formation processes. *J. Climate*, **30**, 9637–9650, https://doi.org/10.1175/JCLI-D-16-0495.1.

Wu, R., Z.-Z. Hu, and B. P. Kirtman, 2003: Evolution of ENSO-related rainfall anomalies in East Asia. *J. Climate*, **16**, 3742–3758, https://doi.org/10.1175/1520-0442(2003)016<3742:EOERAI>2.0.CO;2.

Xiang, B., B. Wang, and T. Li, 2013: A new paradigm for the predominance of standing central Pacific warming after the late 1990s. *Climate Dyn.*, **41**, 327–340, https://doi.org/10.1007/s00382-012-1427-8.

Xie, S.-P., C. Deser, G. A. Vecchi, J. Ma, H. Teng, and A. T. Wittenberg, 2010: Global warming pattern formation: Sea surface temperature and rainfall. *J. Climate*, **23**, 966–986, https://doi.org/10.1175/2009JCLI3329.1.

——, and Coauthors, 2015: Towards predictive understanding of regional climate change. *Nat. Climate Change*, **5**, 921–930, https://doi.org/10.1038/nclimate2689.

Zhang, R. H., Q. Y. Min, and J. Z. Su, 2017: Impact of El Niño on atmospheric circulations over East Asia and rainfall in China: Role of the anomalous western North Pacific anticyclone. *Sci. China Earth Sci.*, **60**, 1124–1132, https://doi.org/10.1007/s11430-016-9026-x.

Zhang, W., F.-F. Jin, J. Li, and H.-L. Ren, 2011: Contrasting impacts of two-type El Niño over the western North Pacific during boreal autumn. *J. Meteor. Soc. Japan*, **89**, 563–569, https://doi.org/10.2151/JMSJ.2011-510.

——, ——, and A. Turner, 2014: Increasing autumn drought over southern China associated with ENSO regime shift. *Geophys. Res. Lett.*, **41**, 4020–4026, https://doi.org/10.1002/2014GL060130.

Zhao, S., H. Zhang, and B. Xie, 2018: The effects of El Niño–Southern Oscillation on the winter haze pollution of China. *Atmos. Chem. Phys.*, **18**, 1863–1877, https://doi.org/10.5194/acp-18-1863-2018.

Zhou, Z.-Q., S.-P. Xie, X.-T. Zheng, Q. Liu, and H. Wang, 2014: Global warming–induced changes in El Niño teleconnections over the North Pacific and North America. *J. Climate*, **27**, 9050–9064, https://doi.org/10.1175/JCLI-D-14-00254.1.

Zong, Y., and X. Chen, 2000: The 1998 flood on the Yangtze, China. *Nat. Hazards*, **22**, 165–184, https://doi.org/10.1023/A:1008119805106.